lifetime of a CH_4 perturbation to the lifetime of the total CH_4 burden, is calculated as f = 1/(1-s). Other CH_4 losses, which are relatively insensitive to CH_4 burden, must be included so that $f = 1.34 \pm 0.06$, (slightly larger but within the range of the Stevenson et al. (2006) estimate of 1.29 ± 0.04, based on six models), leading to an overall perturbation lifetime of 12.4 ± 1.4 years, which is used in calculations of metrics in Section 8.7. Additional details are provided in the Supplementary Material Section 8.SM.2.

8.2.3.4 Nitrous Oxide

Nitrous oxide (N_2O) in 2011 has a surface concentration 19% above its 1750 level (Sections 2.2.1.1.3 and 8.3.2.3). Increases in N_2O lead to depletion of mid- to upper-stratospheric ozone and increase in mid-latitude lower stratospheric ozone (as a result of increased photolysis rate from decreased ozone above). This impacts tropospheric chemistry through increase in stratosphere–troposphere exchange of ozone and odd nitrogen species and increase in tropospheric photolysis rates and OH formation (Prather and Hsu, 2010). Anthropogenic emissions represent around 30 to 45% of the present-day global total, and are mostly from agricultural and soil sources (Fowler et al., 2009) and fossil-fuel activities. Natural emissions come mostly from microbial activity in the soil. The main sink for N_2O is through photolysis and oxidation reactions in the stratosphere, leading to an estimated lifetime of 131 ± 10 years (Prather et al., 2012), slightly larger than previous estimates (Prather and Hsu, 2010; Montzka et al., 2011). The addition of N_2O to the atmosphere changes its own lifetime through feedbacks that couple N_2O to stratospheric NO_y and ozone depletion (Prather, 1998; Ravishankara et al., 2009; Prather and Hsu, 2010), so that the lifetime of a perturbation is less than that of the total burden, 121 ± 10 years (1-σ; Prather et al., 2012) and is used in calculations of metrics (Section 8.7).

8.2.3.5 Halogenated Species

Halogenated species can be powerful greenhouse gases (GHGs). Those containing chlorine and bromine also deplete stratospheric ozone and are referred to as ozone-depleting substances (ODSs). Most of those compounds do not have natural emissions and, because of the implementation of the Montreal Protocol and its amendments, total emissions of ODSs have sharply decreased since the 1990s (Montzka et al., 2011). For CFCs, perfluorocarbons (PFCs) and SF_6 the main loss is through photolysis in the stratosphere. The CFC substitutes (hydrochlorofluorocarbons (HCFCs) and hydrofluorocarbons (HFCs)) are destroyed by OH oxidation in the troposphere. Their global concentration has steadily risen over the recent past (see Section 2.2.1.1.4).

8.2.3.6 Aerosols

Aerosol particles are present in the atmosphere with size ranges from a few nanometres to tens of micrometres. They are the results of direct emission (primary aerosols: BC, OC, sea salt, dust) into the atmosphere or as products of chemical reactions (secondary inorganic aerosols: sulphate, nitrate, ammonium; and secondary organic aerosols (SOAs)) occurring in the atmosphere. Secondary inorganic aerosols are the products of reactions involving sulphur dioxide, ammonia and nitric oxide emissions. SOAs are the result of chemical reactions of non-methane hydrocarbons (and their products) with the hydroxyl radical (OH), ozone, nitrate (NO_3) or photolysis (Hallquist et al., 2009). Thus although many hydrocarbons in the atmosphere are of biogenic origin, anthropogenic pollutants can have impacts on their conversion to SOAs. There is tremendous complexity and still much uncertainty in the processes involved in the formation of SOAs (Hallquist et al., 2009; Carslaw et al., 2010). Additional information can be found in Section 7.3.2.

Once generated, the size and composition of aerosol particles can be modified by additional chemical reactions, condensation or evaporation of gaseous species and coagulation (Seinfeld and Pandis, 2006). It is this set of processes that defines their physical, chemical and optical properties, and hence their impact on radiation and clouds, with large regional and global differences (see Section 7.3.3). Furthermore, their distribution is affected by transport and deposition, defining a residence time in the troposphere of usually a few days (Textor et al., 2006).

8.3 Present-Day Anthropogenic Radiative Forcing

Human activity has caused a variety of changes in different forcing agents in the atmosphere or land surface. A large number of GHGs have had a substantial increase over the Industrial Era and some of these gases are entirely of anthropogenic origin. Atmospheric aerosols have diverse and complex influences on the climate. Human activity has modified the land cover and changed the surface albedo. Some of the gases and aerosols are directly emitted to the atmosphere whereas others are secondary products from chemical reactions of emitted species. The lifetimes of these different forcing agents vary substantially. This section discusses all known anthropogenic forcing agents of non-negligible importance and their quantification in terms of RF or ERF based on changes in abundance over the 1750–2011 period.

In this section we determine the RFs for WMGHGs and heterogeneously distributed species in fundamentally different ways. As described in Box 8.2, the concentrations of WMGHGs can be determined from observations at a few surface sites. For the pre-industrial concentrations these are typically from trapped air in polar ice or firn (see Section 2.2.1). Thus the RFs from WMGHGs are determined entirely from observations (Section 8.3.2). In contrast, we do not have sufficient pre-industrial or present-day observations of heterogeneously distributed forcing agents (e.g., ozone and aerosols) to be able to characterize their RF; therefore we instead have to rely on chemistry–climate models (Sections 8.3.3 and 8.3.4).

8.3.1 Updated Understanding of the Spectral Properties of Greenhouse Gases and Radiative Transfer Codes

RF estimates are performed with a combination of radiative transfer codes typical for GCMs as well as more detailed radiative transfer codes. Physical properties are needed in the radiative transfer codes such as spectral properties for gases. The HITRAN (HIgh Resolution TRANsmission molecular absorption) database (Rothman, 2010) is widely used in radiative transfer models. Some researchers studied

the difference among different editions of HITRAN databases for diverse uses (Feng et al., 2007; Kratz, 2008; Feng and Zhao, 2009; Fomin and Falaleeva, 2009; Lu et al., 2012). Model calculations have shown that modifications of the spectroscopic characteristics tend to have a modest effect on the determination of RF estimates of order 2 to 3% of the calculated RF attributed to the combined doubling of CO_2, N_2O and CH_4. These results showed that even the largest overall RF induced by differences among the HITRAN databases is considerably smaller than the range reported for the modelled RF estimates; thus the line parameter updates to the HITRAN database are not a significant source for discrepancies in the RF calculations appearing in the IPCC reports. However, the more recent HITRAN data set is still recommended, as the HITRAN process offers internal verification and tends to progress closer to the best laboratory measurements. It is found that the differences among the water vapour continuum absorption formulations tend to be comparable to the differences among the various HITRAN databases (Paynter and Ramaswamy, 2011); but use of the older Robert continuum formula produces significantly larger flux differences, thus, replacement of the older continuum is warranted (Kratz, 2008) and there are still numerous unresolved issues left in the continuum expression, especially related to shortwave radiative transfer (Shine et al., 2012). Differences in absorption data from various HITRAN versions are *very likely* a small contributor to the uncertainty in RF of GHGs.

Line-by-line (LBL) models using the HITRAN data set as an input are the benchmark of radiative transfer models for GHGs. Some researchers compared different LBL models (Zhang et al., 2005; Collins et al., 2006) and line-wing cutoff, line-shape function and gas continuum absorption treatment effects on LBL calculations (Zhang et al., 2008; Fomin and Falaleeva, 2009). The agreement between LBL codes has been investigated in many studies and found to generally be within a few percent (e.g., Collins et al., 2006; Iacono et al., 2008; Forster et al., 2011a) and to compare well to observed radiative fluxes under controlled situations (Oreopoulos et al., 2012). Forster et al. (2011a) evaluated global mean radiatively important properties of chemistry climate models (CCMs) and found that the combined WMGHG global annual mean instantaneous RF at the tropopause is within 30% of LBL models for all CCM radiation codes tested. The accuracies of the LW RF due to CO_2 and tropospheric ozone increase are generally very good and within 10% for most of the participation models, but problems remained in simulating RF for stratospheric water vapour and ozone changes with errors between 3% and 200% compared to LBL models. Whereas the differences in the results from CCM radiation codes were large, the agreement among the LW LBL codes was within 5%, except for stratospheric water vapour changes.

Most intercomparison studies of the RF of GHGs are for clear-sky and aerosol-free conditions; the introduction of clouds would greatly complicate the targets of research and are usually omitted in the intercomparison exercises of GCM radiation codes and LBL codes (e.g., Collins et al., 2006; Iacono et al., 2008). It is shown that clouds can reduce the magnitude of RF due to GHGs by about 25% (Forster et al., 2005; Worden et al., 2011; Zhang et al., 2011), but the influence of clouds on the diversity in RF is found to be within 5% in four detailed radiative transfer schemes with realistic cloud distributions (Forster et al., 2005). Estimates of GHG RF are based on the LBL codes or the radiative transfer codes compared and validated against LBL models, and the uncertainty range from AR4 in the RF of GHG of 10% is retained. We underscore that uncertainty in RF calculations in many GCMs is substantially higher owing both to radiative transfer codes and meteorological data such as clouds adopted in the simulations.

8.3.2 Well-mixed Greenhouse Gases

AR4 assessed the RF from 1750 to 2005 of the WMGHGs to be 2.63 W m^{-2}. The four most important gases were CO_2, CH_4, dichlorodifluoromethane (CFC-12) and N_2O in that order. Halocarbons, comprising CFCs, HCFCs, HFCs, PFCs and SF_6, contributed 0.337 W m^{-2} to the total. Uncertainties (90% confidence ranges) were assessed to be approximately 10% for the WMGHGs. The major changes to the science since AR4 are the updating of the atmospheric concentrations, the inclusion of new species (NF_3 and SO_2F_2) and discussion of ERF for CO_2. Since AR4 N_2O has overtaken CFC-12 as the third largest contributor to RF. The total WMGHG RF is now 2.83 (2.54 to 3.12) W m^{-2}.

The RFs in this section are derived from the observed differences in concentrations of the WMGHGs between 1750 and 2011. The concentrations of CO_2, CH_4 and N_2O vary throughout the pre-industrial era, mostly due to varying climate, with a possible small contribution from anthropogenic emissions (MacFarling Meure et al., 2006). These variations do not contribute to uncertainty in the RF as strictly defined here, but do affect the RF attribution to anthropogenic emissions. On centennial time scales, variations in late Holocene concentrations of CO_2 are around 10 ppm (see note to Table 2.1), much larger than the uncertainty in the 1750 concentration. This would equate to a variation in the RF of 10%. For CH_4 and N_2O the centennial variations are comparable to the uncertainties in the 1750 concentrations and so do not significantly affect the estimate of the 1750 value used in calculating RF.

8.3.2.1 Carbon Dioxide

The tropospheric mixing ratio of CO_2 has increased globally from 278 (276–280) ppm in 1750 to 390.5 (390.3 to 390.7) ppm in 2011 (see Section 2.2.1.1.1). Here we assess the RF due to changes in atmospheric concentration rather than attributing it to anthropogenic emissions. Section 6.3.2.6 describes how only a fraction of the historical CO_2 emissions have remained in the atmosphere. The impact of land use change on CO_2 from 1850 to 2000 was assessed in AR4 to be 12 to 35 ppm (0.17 to 0.51 W m^{-2}).

Using the formula from Table 3 of Myhre et al. (1998), and see Supplementary Material Table 8.SM.1, the CO_2 RF (as defined in Section 8.1) from 1750 to 2011 is 1.82 (1.63 to 2.01) W m^{-2}. The uncertainty is dominated by the radiative transfer modelling which is assessed to be 10% (Section 8.3.1). The uncertainty in the knowledge of 1750 concentrations contributes only 2% (see Supplementary Material Table 8.SM.2)

Table 8.2 shows the concentrations and RF in AR4 (2005) and 2011 for the most important WMGHGs. Figure 8.6 shows the time evolution of RF and its rate of change. Since AR4, the RF of CO_2 has increased by 0.16 W m^{-2} and continues the rate noted in AR4 of almost 0.3 W m^{-2} per decade. As shown in Figure 8.6(d) the rate of increase in the RF

from the WMGHGs over the last 15 years has been dominated by CO_2. Since AR4, CO_2 has accounted for more than 80% of the WMGHG RF increase. The interannual variability in the rate of increase in the CO_2 RF is due largely to variation in the natural land uptake whereas the trend is driven by increasing anthropogenic emissions (see Figure 6.8 in Section 6.3.1).

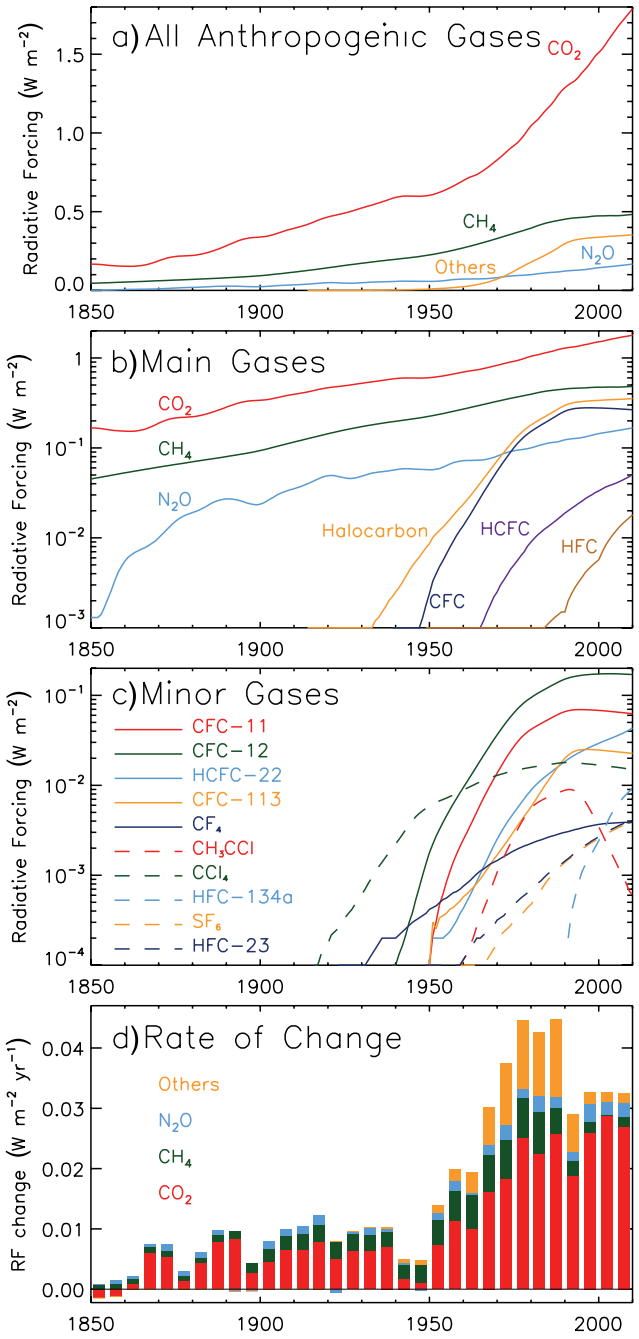

Figure 8.6 | (a) Radiative forcing (RF) from the major well-mixed greenhouse gases (WMGHGs) and groups of halocarbons from 1850 to 2011 (data from Tables A.II.1.1 and A.II.4.16), (b) as (a) but with a logarithmic scale, (c) RF from the minor WMGHGs from 1850 to 2011 (logarithmic scale). (d) Rate of change in forcing from the major WMGHGs and groups of halocarbons from 1850 to 2011.

As described in Section 8.1.1.3, CO_2 can also affect climate through physical effects on lapse rates and clouds, leading to an ERF that will be different from the RF. Analysis of CMIP5 models (Vial et al., 2013) found a large negative contribution to the ERF (20%) from the increase in land surface temperatures which was compensated for by positive contributions from the combined effects on water vapour, lapse rate, albedo and clouds. It is therefore not possible to conclude with the current information whether the ERF for CO_2 is higher or lower than the RF. Therefore we assess the ratio ERF/RF to be 1.0 and assess our uncertainty in the CO_2 ERF to be (–20% to 20%). We have *medium confidence* in this based on our understanding that the physical processes responsible for the differences between ERF and RF are small enough to be covered within the 20% uncertainty.

There are additional effects mediated through plant physiology, reducing the conductance of the plant stomata and hence the transpiration of water. Andrews et al. (2012b) find a physiological enhancement of the adjusted forcing by 3.5% due mainly to reductions in low cloud. This is smaller than a study with an earlier model by Doutriaux-Boucher et al. (2009) which found a 10% effect. Longer-term impacts of CO_2 on vegetation distributions also affect climate (O'ishi et al., 2009; Andrews et al., 2012b) but because of the longer time scale we choose to class these as feedbacks rather than rapid adjustments.

8.3.2.2 Methane

Globally averaged surface CH_4 concentrations have risen from 722 ± 25 ppb in 1750 to 1803 ± 2 ppb by 2011 (see Section 2.2.1.1.2). Over that time scale the rise has been due predominantly to changes in anthropogenic-related CH_4. Anthropogenic emissions of other compounds have also affected CH_4 concentrations by changing its removal rate (Section 8.2.3.3). Using the formula from Myhre et al. (1998) (see Supplementary Material Table 8.SM.1) the RF for CH_4 from 1750 to 2011 is 0.48 ± 0.05 W m^{-2}, with an uncertainty dominated by the radiative transfer calculation. This increase of 0.01 W m^{-2} since AR4 is due to the 29 ppb increase in the CH_4 mixing ratio. This is much larger than the 11 ppb increase between TAR and AR4, and has been driven by increases in net natural and anthropogenic emissions, but the relative contributions are not well quantified. Recent trends in CH_4 and their causes are discussed in Sections 2.2.1.1.2 and 6.3.3.1. CH_4 concentrations do vary with latitude and decrease above the tropopause; however, this variation contributes only 2% to the uncertainty in RF (Freckleton et al., 1998).

In this section only the direct forcing from changing CH_4 concentrations is addressed. CH_4 emissions can also have indirect effects on climate through impacts on CO_2, stratospheric water vapour, ozone, sulphate aerosol and lifetimes of HFCs and HCFCs (Boucher et al., 2009; Shindell et al., 2009; Collins et al., 2010). Some of these are discussed further in Sections 8.3.3, 8.5.1 and 8.7.2.

8.3.2.3 Nitrous Oxide

Concentrations of nitrous oxide have risen from 270 ± 7 ppb in 1750 to 324.2 ± 0.1 ppb in 2011, an increase of 5 ppb since 2005 (see Section 2.2.1.1.3). N_2O now has the third largest forcing of the anthropogenic gases, at 0.17 ± 0.03 W m^{-2} an increase of 6% since 2005 (see Table

8.2) where the uncertainty is due approximately equally to the pre-industrial concentration and radiative transfer. Only the direct RF from changing nitrous oxide concentrations is included. Indirect effects of N_2O emissions on stratospheric ozone are not taken into account here but are discussed briefly in Section 8.7.2.

8.3.2.4 Other Well-mixed Greenhouse Gases

RFs of the other WMGHG are shown in Figure 8.6 (b and c) and Table 8.2. The contribution of groups of halocarbons to the rate of change of WMGHG RF is shown in Figure 8.6 (d). Between 1970 and 1990 halocarbons made a significant contribution to the rate of change of RF. The rate of change in the total WMGHG RF was higher in 1970 to 1990 with *high confidence* compared to the present owing to higher contribution from non-CO_2 gases especially the halocarbons. Since the Montreal Protocol and its amendments, the rate of change of RF from halocarbons and related compounds has been much less, but still just positive (total RF of 0.360 W m^{-2} in 2011 compared to 0.351 W m^{-2} in 2005) as the growth of HCFCs, HFCs, PFCs and other halogens (SF_6, SO_2F_2, NF_3) RFs (total 0.022 W m^{-2} since 2005) more than compensates

Table 8.2 | Present-day mole fractions (in ppt(pmol mol^{-1}) except where specified) and RF (in W m^{-2}) for the WMGHGs. Concentration data are averages of National Oceanic and Atmospheric Administration (NOAA) and Advanced Global Atmospheric Gases Experiment (AGAGE) observations where available. CO_2 concentrations are the average of NOAA and SIO. See Table 2.1 for more details of the data sources. The data for 2005 (the time of the AR4 estimates) are also shown. Some of the concentrations vary slightly from those reported in AR4 owing to averaging different data sources. Radiative efficiencies for the minor gases are given in Table 8.A.1. Uncertainties in the RF for all gases are dominated by the uncertainties in the radiative efficiencies. We assume the uncertainties in the radiative efficiencies to be perfectly correlated between the gases, and the uncertainties in the present day and 1750 concentrations to be uncorrelated.

	Concentrations (ppt)		Radiative forcing[a] (W m^{-2})	
Species	**2011**	**2005**	**2011**	**2005**
CO_2 (ppm)	391 ± 0.2	379	1.82 ± 0.19	1.66
CH_4 (ppb)	1803 ± 2	1774	0.48 ± 0.05	0.47[e]
N_2O (ppb)	324 ± 0.1	319	0.17 ± 0.03	0.16
CFC-11	238 ± 0.8	251	0.062	0.065
CFC-12	528 ± 1	542	0.17	0.17
CFC-13	2.7		0.0007	
CFC-113	74.3 ± 0.1	78.6	0.022	0.024
CFC-115	8.37	8.36	0.0017	0.0017
HCFC-22	213 ± 0.1	169	0.0447	0.0355
HCFC-141b	21.4 ± 0.1	17.7	0.0034	0.0028
HCFC-142b	21.2 ± 0.2	15.5	0.0040	0.0029
HFC-23	24.0 ± 0.3	18.8	0.0043	0.0034
HFC-32	4.92	1.15	0.0005	0.0001
HFC-125	9.58 ± 0.04	3.69	0.0022	0.0008
HFC-134a	62.7 ± 0.3	34.3	0.0100	0.0055
HFC-143a	12.0 ± 0.1	5.6	0.0019	0.0009
HFC-152a	6.4 ± 0.1	3.4	0.0006	0.0003
SF_6	7.28 ± 0.03	5.64	0.0041	0.0032
SO_2F_2	1.71	1.35	0.0003	0.0003
NF_3	0.9	0.4	0.0002	0.0001
CF_4	79.0 ± 0.1	75.0	0.0040	0.0036
C_2F_6	4.16 ± 0.02	3.66	0.0010	0.0009
CH_3CCl_3	6.32 ± 0.07	18.32	0.0004	0.0013
CCl_4	85.8 ± 0.8	93.1	0.0146	0.0158
CFCs			0.263 ± 0.026[b]	0.273[c]
HCFCs			0.052 ± 0.005	0.041
Montreal gases[d]			0.330 ± 0.033	0.331
Total halogens			0.360 ± 0.036	0.351[f]
Total			2.83 ± 0.029	2.64

Notes:

[a] Pre-industrial values are zero except for CO_2 (278 ppm), CH_4 (722 ppb), N_2O (270 ppb) and CF_4 (35 ppt).

[b] Total includes 0.007 W m^{-2} to account for CFC-114, Halon-1211 and Halon-1301.

[c] Total includes 0.009 W m^{-2} forcing (as in AR4) to account for CFC-13, CFC-114, CFC-115, Halon-1211 and Halon-1301.

[d] Defined here as CFCs + HCFCs + CH_3CCl_3 + CCl_4.

[e] The value for the 1750 methane concentrations has been updated from AR4 in this report, thus the 2005 methane RF is slightly lower than reported in AR4.

[f] Estimates for halocarbons given in the table may have changed from estimates reported in AR4 owing to updates in radiative efficiencies and concentrations.

for the decline in the CFCs, CH_3CCl_3 and CCl_4 RFs (–0.013 W m^{-2} since 2005). The total halocarbon RF is dominated by four gases, namely CFC-12, trichlorofluoromethane (CFC-11), chlorodifluoromethane (HCFC-22) and trichlorofluoroeethane (CFC-113) in that order, which account for about 85% of the total halocarbon RF (see Table 8.2) . The indirect RF from the impacts of ODSs is discussed in Section 8.3.3.2.

8.3.2.4.1 Chlorofluorocarbons and hydrochlorofluorocarbons

The CFCs and HCFCs contribute approximately 11% of the WMGHG RF. Although emissions have been drastically reduced for CFCs, their long lifetimes mean that reductions take substantial time to affect their concentrations. The RF from CFCs has declined since 2005 (mainly due to a reduction in the concentrations of CFC-11 and CFC-12), whereas the RF from HCFCs is still rising (mainly due to HCFC-22).

8.3.2.4.2 Hydrofluorocarbons

The RF of HFCs is 0.02 W m^{-2} and has close to doubled since AR4 (2005 concentrations). HFC-134a is the dominant contributor to RF of the HFCs, with an RF of 0.01 W m^{-2}.

8.3.2.4.3 Perfluorocarbons and sulphur hexafluoride

These gases have lifetimes of thousands to tens of thousands of years (Table 8.A.1); therefore emissions essentially accumulate in the atmosphere on the time scales considered here. CF_4 has a natural source and a 1750 concentration of 35 ppt (see Section 2.2.1.1.4). These gases currently contribute 0.01 W m^{-2} of the total WMGHG RF.

8.3.2.4.4 New species

Nitrogen trifluoride (NF_3) is used in the electronics industry and sulfuryl fluoride (SO_2F_2) is used as a fumigant. Both have rapidly increasing emissions and high GWPs, but currently contribute only around 0.0002 W m^{-2} and 0.0003 W m^{-2} to anthropogenic RF, respectively (Weiss et al., 2008; Andersen et al., 2009; Muhle et al., 2009; Arnold et al., 2013).

8.3.3 Ozone and Stratospheric Water Vapour

Unlike for the WMGHGs, the estimate of the tropospheric and stratospheric ozone concentration changes are almost entirely model based for the full pre-industrial to present-day interval (though, especially for the stratosphere, more robust observational evidence on changes is available for recent decades; see Section 2.2).

AR4 assessed the RF (for 1750–2005) from tropospheric ozone to be 0.35 W m^{-2} from multi-model studies with a high 95th percentile of 0.65 W m^{-2} to allow for the possibility of model overestimates of the pre-industrial tropospheric ozone levels. The stratospheric ozone RF was assessed from observational trends from 1979 to 1998 to be –0.05 ± 0.1 W m^{-2}, with the 90% confidence range increased to reflect uncertainty in the trend prior to 1979 and since 1998. In AR4 the RF from stratospheric water vapour generated by CH_4 oxidation was assessed to be +0.07 ± 0.05 W m^{-2} based on Hansen et al. (2005).

Since AR4, there have been a few individual studies of tropospheric or stratospheric ozone forcing (Shindell et al., 2006a, 2006c, 2013a; Skeie et al., 2011a; Søvde et al., 2011), a multi-model study of stratospheric ozone RF in the 2010 WMO stratospheric ozone assessment (Forster et al., 2011b), and the ACCMIP multi-model study of tropospheric and tropospheric + stratospheric chemistry models (Conley et al., 2013; Stevenson et al., 2013). There is now greater understanding of how tropospheric ozone precursors can affect stratospheric ozone, and how ODSs can affect tropospheric ozone (Shindell et al., 2013a). We assess the total ozone RF to be +0.35 (0.15 to 0.55) W m^{-2}. This can be split according to altitude or by emitted species (Shindell et al., 2013a). We assess these contributions to be 0.40 (0.20 to 0.60) W m^{-2} for ozone in the troposphere and –0.05 ± 0.10 W m^{-2} for ozone in the stratosphere based on the studies presented in Table 8.3. Alternatively, the contributions to the total ozone forcing can be attributed as 0.50 (0.30 to 0.70) W m^{-2} from ozone precursors and –0.15 (–0.3 to 0.0) W m^{-2} from the effect of ODSs. The value attributed to ODSs is assessed to be slightly smaller in magnitude than in the two studies quoted in Table 8.3 (Søvde et al., 2011; Shindell et al., 2013a) because the models used for these had stratospheric ozone RFs with higher magnitudes than the ACCMIP mean (Conley et al., 2013). Differences between the ERFs and RFs for tropospheric and stratospheric ozone are *likely* to be small compared to the uncertainties in the RFs (Shindell et al., 2013b), so the assessed values for the ERFs are the same as those for the RFs.

The influence of climate change is typically included in ozone RF estimates as those are based on modelled concentration changes, but the available literature provides insufficient evidence for the sign and magnitude of the impact and we therefore refrain from giving an estimate except to assess that it is *very likely* to be smaller than the overall uncertainty in the total RF. Unlike the WMGHGs, there are significant latitudinal variations in the RFs from changes in tropospheric and stratospheric ozone. The implications of inhomogeneous RFs are explored in more detail in Section 8.6.

There has been one study since AR4 (Myhre et al., 2007) on the RF from water vapour formed from the stratospheric oxidation of CH_4 (Section 8.3.3.3). This is consistent with the AR4 value and so has not led to any change in the recommended value of 0.07 (0.02 to 0.12) W m^{-2} since AR4.

8.3.3.1 Tropospheric Ozone

Ozone is formed in the troposphere by photochemical reactions of natural and anthropogenic precursor species (Section 8.2.3.1). Changes in ozone above the tropopause due to emissions of stratospheric ODSs can also affect ozone in the troposphere either by transport across the tropopause or modification of photolysis rates. Changes in climate have also affected tropospheric ozone concentrations (medium evidence, low agreement) through changes in chemistry, natural emissions and transport from the stratosphere (Isaksen et al., 2009).

The most recent estimates of tropospheric ozone RF come from multi-model studies under ACCMIP (Conley et al., 2013; Lamarque et al., 2013; Stevenson et al., 2013). The model ensemble reported only 1850–2000 RFs (0.34 W m^{-2}) so the single-model results from Skeie et

al. (2011a) were used to expand the timespan to 1750–2010, adding 0.04 W m^{-2}, and 0.02 W m^{-2} to account for the periods 1750–1850 and 2000–2010 respectively. The best estimate of tropospheric ozone RF taking into account the ACCMIP models and the Søvde et al. (2011) results (the Skeie et al. (2011a) and Shindell et al. (2013a) models are included in ACCMIP) is 0.40 (0.20 to 0.60) W m^{-2}. The quantifiable uncertainties come from the inter-model spread (–0.11 to 0.11 W m^{-2}) and the differences between radiative transfer models (–0.07 to 0.07 W m^{-2}); all 5 to 95% confidence interval. Additional uncertainties arise from the lack of knowledge of pre-industrial emissions and the representation of chemical and physical processes beyond those included in the current models. The tropospheric ozone RF is sensitive to the assumed 'pre-industrial' levels. As described in Section 8.2.3.1, very limited late 19th and early 20th century observations of surface ozone concentrations are lower than the ACCMIP models for the same period; however, we assess that those observations are very uncertain. Skeie et al. (2011a) and Stevenson et al. (2013) increase their uncertainty ranges to 30% for 1 standard deviation which is equivalent to (–50% to +50%) for the 5 to 95% confidence range and we adopt this for AR5. The overall *confidence* in the tropospheric ozone RF is assessed as *high*.

Because we have *low confidence* in the pre-industrial ozone observations, and these were extremely limited in spatial coverage, it is not possible to calculate a purely observationally based ozone RF. However, modern observations can be used to assess the performance of the chemistry models. Bowman et al. (2013) used satellite retrievals from the TES instrument to constrain the RF from the ACCMIP models. This reduced the inter-model uncertainty by 30%; however, we still maintain overall the (–50% to +50%) 5 to 95% confidence range for AR5.

The time evolution of the tropospheric ozone forcing is shown in Figure 8.7. There is a noticeable acceleration in the forcing after 1950 and a deceleration in the 1990s reflecting the time evolution of anthropogenic precursor emissions. Observational evidence for trends in ozone concentrations is discussed in Section 2.2.2.3.

It can be useful to calculate a normalized radiative forcing (NRF) which is an RF per change in ozone column in W m^{-2} DU^{-1} or W mol^{-1}. This is only an approximation as the NRF is sensitive to the vertical profile of the ozone change and to the latitudinal profile to a smaller extent. From Table 8.3 we assess the NRF to be 0.042 (0.037 to 0.047) W m^{-2} DU^{-1} (94 (83 to 105) W mol^{-1}) similar to the value of 0.042 W m^{-2} DU^{-1} (94 W mol^{-1}) in TAR (Ramaswamy et al., 2001).

A small number of studies have looked at attributing the ozone changes among the anthropogenically emitted species. Søvde et al. (2011) report a tropospheric ozone RF of 0.38 W m^{-2}, 0.44 W m^{-2} from ozone precursors and –0.06 W m^{-2} from the impact of stratospheric ozone depletion on the troposphere. Shindell et al. (2013a) also calculate that ODSs are responsible for about –0.06 W m^{-2} of the tropospheric ozone RF, and ozone precursors for about 0.41 W m^{-2}. Six of the models in Stevenson et al. (2013) and Shindell et al. (2009) performed experiments to attribute the ozone RF to the individual precursor emissions. An average of these seven model results leads to attributions of 0.24 ± 0.13 W m^{-2} due to CH_4 emissions, 0.14 ± 0.09 W m^{-2} from NO_x emissions, 0.07 ± 0.03 W m^{-2} from CO, and 0.04 ± 0.03W m^{-2} from non-methane volatile organic compounds (NMVOCs). These results were calculated by reducing the precursor emissions individually from 2000 to pre-industrial levels. The results were scaled by the total ozone RFs attributed to ozone precursors (0.50 W m^{-2}) to give the contributions to the full 1750–2010 RF. Because of the nonlinearity of the chemistry an alternative method of starting from pre-industrial conditions and increasing precursor emissions singly may give a different result. Note that as well as inducing an ozone RF, these ozone precursor species can also strongly affect the concentrations of CH_4 and aerosols, adding extra terms (both positive and negative) to their total indirect forcings. The contributions to the 1750–2010 CH_4 RF are again based on Stevenson et al. (2013) and Shindell et al. (2009). The Stevenson et al. (2013) values are for 1850–2000 rather than 1750 to 2011 so for these we distribute the CH_4 RF for 1750–1850 and 2000–2011 (0.06 W m^{-2}) by scaling the CH_4 and CO contributions (assuming these were the most significant contributors over those time periods). This gives contributions of 0.58 ± 0.08, –0.29 ± 0.18, 0.07 ± 0.02 and 0.02 ± 0.02 W m^{-2} for changes from historical to present day emissions of CH_4 (inferred emissions), NO_x, CO and VOCs respectively (uncertainties are 5 to 95% confidence intervals). The difference between the total CH_4 RF attributed to ozone precursors here (0.38 W m^{-2}) and the value calculated from CH_4 concentration changes in Table 8.2 (0.48 W m^{-2}) is due to nonlinearities in the CH_4 chemistry because large single-step changes were used. To allow an easier comparison between the concentration-based and emission-based approaches in Section 8.5.1 the nonlinear term (+0.1 W m^{-2}) is distributed between the four emitted species according to their absolute magnitude so that they total 0.48 W m^{-2}. The scaled results still lie within the uncertainty bounds of the values quoted above. The impact of climate change over the historical period on CH_4 oxidation is not accounted for in these calculations.

Tropospheric ozone can also affect the natural uptake of CO_2 by decreasing plant productivity (see Sections 6.4.8.2 and 8.2.3.1) and it is found that this indirect effect could have contributed to the total CO_2 RF (Section 8.3.2.1; Sitch et al., 2007), roughly doubling the overall RF attributed to ozone precursors. Although we assess there to be

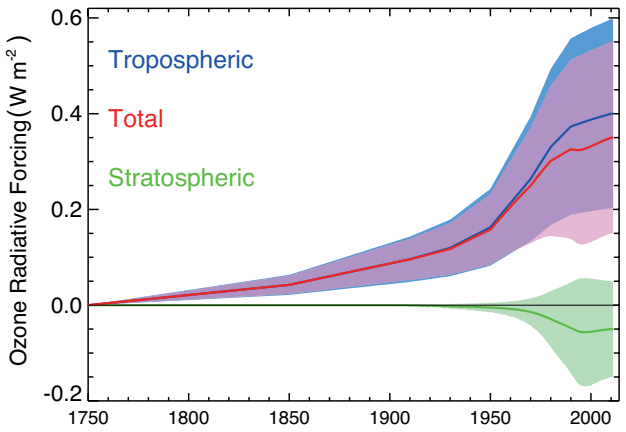

Figure 8.7 | Time evolution of the radiative forcing from tropospheric and stratospheric ozone from 1750 to 2010. Tropospheric ozone data are from Stevenson et al. (2013) scaled to give 0.40 W m^{-2} at 2010. The stratospheric ozone RF follow the functional shape of the Effective Equivalent Stratospheric Chlorine assuming a 3-year age of air (Daniel et al., 2010) scaled to give –0.05 W m^{-2} at 2010.

Table 8.3 | Contributions of tropospheric and stratospheric ozone changes to radiative forcing (W m^{-2}) from 1750 to 2011.

	Troposphere				Stratosphere		
	Longwave	Shortwave	Total	Normalized Radiative Forcing m W m^{-2} DU^{-1}	Longwave	Shortwave	Total
AR4 (Forster et al. (2007)			0.35 (0.25 to 0.65)				–0.05 (–0.15 to 0.05)
Shindell et al. (2013a)[f]			0.33 (0.31 to 0.35)				–0.08 (–0.10 to –0.06)
WMO (Forster et al., 2011b)							–0.03[a] (–0.23 to +0.17) +0.03[b]
Søvde et al. (2011)			0.45[c] 0.38[d]	40 39			–0.12 –0.12
Skeie et al. (2011a)			0.41 (0.21 to 0.61)	38			
ACCMIP[e]	0.33 (0.24 to 0.42)	0.08 (0.06 to 0.10)	0.41 (0.21 to 0.61)	42 (37 to 47)	–0.13 (–0.26 to 0)	0.11 (0.03 to 0.19)	–0.02 (–0.09 to 0.05)
AR5			0.40 (0.20 to 0.60)	42 (37 to 47)			–0.05 (-0.15 to 0.05)

Notes:

[a] From multi-model results.

[b] From Randel and Wu (2007) observation-based data set.

[c] Using the REF chemistry, see Søvde et al. (2011).

[d] Using the R2 chemistry.

[e] The Atmospheric Chemistry and Climate Model Intercomparison Project (ACCMIP) tropospheric ozone RFs are from Stevenson et al. (2013). The stratospheric ozone values are from Conley et al. (2013) calculations for 1850–2005 disregarding the Modèle de Chimie Atmosphérique a Grande Echelle (MOCAGE) model which showed excessive ozone depletion.

[f] Only the Goddard Institute for Space Studies (GISS)-E2-R results (including bias correction) from the Shindell et al. (2013a) study are shown here rather than the multi-model result presented in that paper.

robust evidence of an effect, we make no assessment of the magnitude because of lack of further corroborating studies.

8.3.3.2 Stratospheric Ozone

The decreases in stratospheric ozone due to anthropogenic emissions of ODSs have a positive RF in the shortwave (increasing the flux into the troposphere) and a negative RF in the longwave. This leaves a residual forcing that is the difference of two larger terms. In the lower stratosphere the longwave effect tends to be larger, whereas in the upper stratosphere the shortwave dominates. Thus whether stratospheric ozone depletion has contributed an overall net positive or negative forcing depends on the vertical profile of the change (Forster and Shine, 1997). WMO (2011) assessed the RF from 1979 to 2005 from observed ozone changes (Randel and Wu, 2007) and results from 16 models for the 1970s average to 2004. The observed and modelled mean ozone changes gave RF values of different signs (see Table 8.3). Negative net RFs arise from models with ozone decline in the lowermost stratosphere, particularly at or near the tropopause.

The ACCMIP study also included some models with stratospheric chemistry (Conley et al., 2013). One model in that study stood out as having excessive ozone depletion. Removing that model leaves a stratospheric ozone RF of –0.02 (–0.09 to 0.05) W m^{-2}. These results are in good agreement with the model studies from WMO (2011). Forster et al. (2007) in AR4 calculated a forcing of –0.05 W m^{-2} from observations over the period 1979–1998 and increased the uncertainty to 0.10 W m^{-2} to encompass changes between the pre-industrial period and 2005. The RF from stratospheric ozone due to changes in emissions of ozone precursors and ODSs is here assessed to be –0.05 (–0.15 to 0.05) taking into account all the studies listed in Table 8.3. This is in agreement with AR4, although derived from different data. The timeline of stratospheric ozone forcing is shown in Figure 8.7, making the assumption that it follows the trajectory of the changes in EESC. It reaches a minimum in the late 1990s and starts to recover after that.

The net global RF from ODSs taking into account the compensating effects on ozone and their direct effects as WMGHGs is 0.18 (0.03 to 0.33) W m^{-2}. The patterns of RF for these two effects are different so the small net global RF comprises areas of positive and negative RF.

8.3.3.3 Stratospheric Water Vapour

Stratospheric water vapour is dependent on the amount entering from the tropical troposphere and from direct injection by volcanic plumes (Joshi and Jones, 2009) and aircraft, and the *in situ* chemical production from the oxidation of CH_4 and hydrogen. This contrasts with tropospheric water vapour which is almost entirely controlled by the balance between evaporation and precipitation (see FAQ 8.1). We consider trends in the transport (for instance, due to the Brewer–Dobson circulation or tropopause temperature changes) to be climate feedback rather than a forcing so the anthropogenic RFs come from oxidation of CH_4 and hydrogen, and emissions from stratospheric aircraft.

Myhre et al. (2007) used observations of the vertical profile of CH_4 to deduce a contribution from oxidation of anthropogenic CH_4 of 0.083

W m^{-2} which compares with the value of 0.07 W m^{-2} from calculations in a 2D model in Hansen et al. (2005). Both of these values are consistent with AR4 which obtained the stratospheric water vapour forcing by scaling the CH_4 direct forcing by 15%. Thus the time evolution of this forcing is also obtained by scaling the CH_4 forcing by 15%. The best estimate and uncertainty range from AR4 of 0.07 (0.02 to 0.12) W m^{-2} remain unchanged and the large uncertainty range is due to large differences found in the intercomparison studies of radiative transfer modelling for changes in stratospheric water vapour (see Section 8.3.1).

RF from the current aircraft fleet through stratospheric water vapour emissions is very small. Wilcox et al. (2012) estimate a contribution from civilian aircraft in 2005 of 0.0009 (0.0003 to 0.0013) W m^{-2} with *high confidence* in the upper limit. Water vapour emissions from aircraft in the troposphere also contribute to contrails which are discussed in Section 8.3.4.5.

8.3.4 Aerosols and Cloud Effects

8.3.4.1 Introduction and Summary of AR4

In AR4 (Forster et al., 2007), RF estimates were provided for three aerosol effects. These were the RF of aerosol–radiation interaction (previously denoted as direct aerosol effect), RF of the aerosol–cloud interaction (previously denoted as the cloud albedo effect), and the impact of BC on snow and ice surface albedo. See Chapter 7 and Figure 7.3 for an explanation of the change in terminology between AR4 and AR5. The RF due to aerosol–radiation interaction is scattering and absorption of shortwave and longwave radiation by atmospheric aerosols. Several different aerosol types from various sources are present in the atmosphere (see Section 8.2). Most of the aerosols primarily scatter solar radiation, but some components absorb solar radiation to various extents with BC as the most absorbing component. RF of aerosols in the troposphere is often calculated at the TOA because it is similar to tropopause values (Forster et al., 2007). A best estimate RF of –0.5 ± 0.4 W m^{-2} was given in AR4 for the change in the net aerosol–radiation interaction between 1750 and 2005 and a medium to low level of scientific understanding (LOSU).

An increase in the hygroscopic aerosol abundance may enhance the concentration of cloud condensation nuclei (CCN). This may increase the cloud albedo and under the assumption of fixed cloud water content this effect was given a best estimate of –0.7 W m^{-2} (range from –1.8 to –0.3) in AR4 and a low LOSU.

BC in the snow or ice can lead to a decrease of the surface albedo. This leads to a positive RF. In AR4 this mechanism was given a best RF estimate of 0.1 ± 0.1 W m^{-2} and a low LOSU.

Impacts on clouds from the ERF of aerosol–cloud interaction (including both effects previously denoted as cloud lifetime and cloud albedo effect) and the ERF of aerosol–radiation interaction (including both effects previously denoted as direct aerosol effect and semi-direct effect) were not strictly in accordance with the RF concept, because they involve tropospheric changes in variables other than the forcing agent at least in the available model estimates, so no best RF estimates were provided in AR4 (see Section 8.1). However, the ERF of aerosol–cloud and aerosol–radiation interactions were included in the discussion of total aerosol effect in Chapter 7 in AR4 (Denman et al., 2007). The mechanisms influenced by anthropogenic aerosol including the aerosol cloud interactions are discussed in detail in this assessment in Section 7.5 and summarized in the subsections that follow.

8.3.4.2 Radiation Forcing of the Aerosol–Radiation Interaction by Component

Based on a combination of global aerosol models and observation-based methods, the best RF estimate of the aerosol–radiation interaction in AR5 is –0.35 (–0.85 to +0.15) W m^{-2} (see Section 7.5). This estimate is thus smaller in magnitude than in AR4, however; with larger uncertainty range. Overall, the estimate compared to AR4 is more robust because the agreement between estimates from models and observation-based methods is much greater (see Section 7.5). The larger range arises primarily from analysis by observation-based methods (see Section 7.5).

The main source of the model estimate is based on updated simulations in AeroCom (Myhre et al., 2013), which is an intercomparison exercise of a large set of global aerosol models that includes extensive evaluation against measurements. The assessment in Chapter 7 relies to a large extent on this study for the separation in the various aerosol components, except for BC where the assessment in Chapter 7 relies in addition on Bond et al. (2013). The RF of aerosol–radiation interaction is separated into seven components in this report; namely sulphate, BC from fossil fuel and biofuel, OA from fossil fuel and biofuel, BC and OA combined from biomass burning (BB), nitrate, SOA and mineral dust. BC and OA from biomass burning are combined due to the joint sources, whereas treated separately for fossil fuel and biofuel because there is larger variability in the ratio of BC to OA in the fossil fuel and biofuel emissions. This approach is consistent with TAR and AR4. Table 8.4 compares the best estimates of RF due to aerosol–radiation interaction for various components in this report with values in SAR, TAR and AR4. In magnitude the sulphate and BC from use of fossil fuel and biofuel dominate. It is important to note that the BB RF is small in magnitude but consists of larger, offsetting terms in magnitude from OA and BC (see Section 7.5.2). Changes in the estimates of RF due to aerosol–radiation interaction of the various components have been rather modest compared to AR4, except for BC from fossil fuel and biofuel (see Section 7.5). SOA is a new component compared to AR4. Anthropogenic SOA precursors contribute only modestly to the anthropogenic change in SOA. The increase in SOA is mostly from biogenic precursors and enhanced partitioning of SOA into existing particles from anthropogenic sources and changes in the atmospheric oxidation (Carlton et al., 2010). This change in SOA is therefore of anthropogenic origin, but natural emission of SOA precursors is important (Hoyle et al., 2011).

Note that the best estimate and the uncertainty for the total is not equal to the sum of the aerosol components because the total is estimated based on a combination of methods (models and observation-based methods), whereas the estimates for the components rely mostly on model estimates.

Table 8.4 | Global and annual mean RF (W m^{-2}) due to aerosol–radiation interaction between 1750 and 2011 of seven aerosol components for AR5. Values and uncertainties from SAR, TAR, AR4 and AR5 are provided when available. Note that for SAR, TAR and AR4 the end year is somewhat different than for AR5 with 1993, 1998 and 2005, respectively.

	Global Mean Radiative Forcing (W m^{-2})			
	SAR	TAR	AR4	AR5
Sulphate aerosol	–0.40 (–0.80 to –0.20)	–0.40 (–0.80 to –0.20)	–0.40 (–0.60 to –0.20)	–0.40 (–0.60 to –0.20)
Black carbon aerosol from fossil fuel and biofuel	+0.10 (+0.03 to +0.30)	+0.20 (+0.10 to +0.40)	+0.20 (+0.05 to +0.35)	+0.40 (+0.05 to +0.80)
Primary organic aerosol from fossil fuel and biofuel	Not estimated	–0.10 (–0.30 to –0.03)	–0.05 (0.00 to –0.10)	–0.09 (–0.16 to –0.03)
Biomass burning	–0.20 (–0.60 to –0.07)	–0.20 (–0.60 to –0.07)	+0.03(–0.09 to +0.15)	–0.0 (–0.20 to +0.20)
Secondary organic aerosol	Not estimated	Not estimated	Not estimated	–0.03 (–0.27 to +0.20)
Nitrate	Not estimated	Not estimated	–0.10 (–0.20 to 0.00)	–0.11 (–0.30 to –0.03)
Dust	Not estimated	–0.60 to +0.40	–0.10 (–0.30 to +0.10)	–0.10 (–0.30 to +0.10)
Total	Not estimated	Not estimated	–0.50 (–0.90 to –0.10)	–0.35 (–0.85 to +0.15)

The RF due to aerosol–radiation interaction during some time periods is more uncertain than the current RF. Improvements in the observations of aerosols have been substantial with availability of remote sensing from the ground-based optical observational network AErosol RObotic NETwork (AERONET) and the launch of the Moderate Resolution Imaging Spectrometer (MODIS) and Multi-angle Imaging Spectro-Radiometer (MISR) instruments (starting in 2000) as well as other satellite data. This has contributed to constraining the current RF using aerosol observations. The aerosol observations are very limited backward in time, although there is growing constraint coming from new ice and lake core records, and uncertainties in the historical emission of aerosols and their precursors used in the global aerosol modeling are larger than for current conditions. Emissions of carbonaceous aerosols are particularly uncertain in the 1800s due to a significant biofuel source in this period, in contrast to the SO_2 emissions which were very small until the end of the 1800s. The uncertainty in the biomass burning emissions also increases backward in time. Note that, for 1850, the biomass burning emissions from Lamarque et al. (2010) are quite different from the previous estimates, but RF due to aerosol–radiation interaction is close to zero for this component. Figure 8.8 shows an example of the time evolution of the RF due to aerosol–radiation interaction as a total and separated into six aerosol components. From 1950 to 1990 there was a strengthening of the total RF due to aerosol–radiation interaction, mainly due to a strong enhancement of the sulphate RF. After 1990 the change has been small with even a weakening of the RF due to aerosol–radiation interaction, mainly due to a stronger BC RF as a result of increased emissions in East and Southeast Asia.

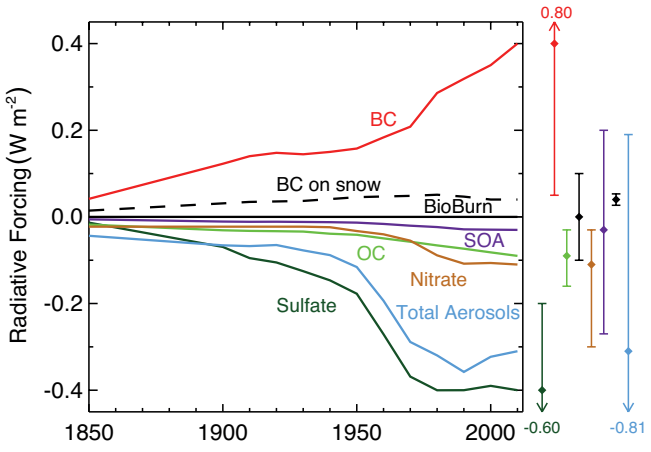

Figure 8.8 | Time evolution of RF due to aerosol–radiation interaction and BC on snow and ice. Multi-model results for 1850, 1930, 1980 and 2000 from ACCMIP for aerosol–radiation interaction (Shindell et al., 2013c) and BC on snow and ice (Lee et al., 2013) are combined with higher temporal-resolution results from the Goddard Institute for Space Studies (GISS)-E2 and Oslo-Chemical Transport Model 2 (OsloCTM2) models (aerosol–radiation interaction) and OsloCTM2 (BC on snow and ice). Uncertainty ranges (5 to 95%) for year 2010 are shown with vertical lines. Values next to the uncertainty lines are for cases where uncertainties go beyond the scale. The total includes the RF due to aerosol–radiation interaction for six aerosol components and RF due to BC on snow and ice. All values have been scaled to the best estimates for 2011 given in Table 8.4. Note that time evolution for mineral dust is not included and the total RF due to aerosol–radiation interaction is estimated based on simulations of the six other aerosol components.

8.3.4.3 Aerosol–Cloud Interactions

The RF by aerosol effects on cloud albedo was previously referred to as the Twomey or cloud albedo effect (see Section 7.1). Although this RF can be calculated, no estimate of this forcing is given because it has heuristic value only and does not simply translate to the ERF due to aerosol–cloud interaction. The total aerosol ERF, namely ERF due to aerosol–radiation and aerosol–cloud interactions (excluding BC on snow and ice) provided in Chapter 7 is estimated with a 5 to 95% uncertainty between –1.9 and –0.1 W m^{-2} with a best estimate value of –0.9 W m^{-2} (*medium confidence*). The *likely* range of this forcing is between –1.5 and –0.4 W m^{-2}. The estimate of ERF due to aerosol–radiation and aerosol-cloud interaction is lower (i.e., less negative) than the corresponding AR4 RF estimate of –1.2 W m^{-2} because the latter was based mainly on GCM studies that did not take secondary processes (such as aerosol effects on mixed-phase and/or convective clouds and effects on longwave radiation) into account. This new best estimate of ERF due to aerosol–radiation and aerosol–cloud interaction is also consistent with the studies allowing cloud-scale processes and related responses and with the lower estimates of this forcing inferred from satellite observations.

Frequently Asked Questions

FAQ 8.2 | Do Improvements in Air Quality Have an Effect on Climate Change?

Yes they do, but depending on which pollutant(s) they limit, they can either cool or warm the climate. For example, whereas a reduction in sulphur dioxide (SO_2) emissions leads to more warming, nitrogen oxide (NO_x) emission control has both a cooling (through reducing of tropospheric ozone) and a warming effect (due to its impact on methane lifetime and aerosol production). Air pollution can also affect precipitation patterns.

Air quality is nominally a measure of airborne surface pollutants, such as ozone, carbon monoxide, NO_x and aerosols (solid or liquid particulate matter). Exposure to such pollutants exacerbates respiratory and cardiovascular diseases, harms plants and damages buildings. For these reasons, most major urban centres try to control discharges of airborne pollutants.

Unlike carbon dioxide (CO_2) and other well-mixed greenhouse gases, tropospheric ozone and aerosols may last in the atmosphere only for a few days to a few weeks, though indirect couplings within the Earth system can prolong their impact. These pollutants are usually most potent near their area of emission or formation, where they can force local or regional perturbations to climate, even if their globally averaged effect is small.

Air pollutants affect climate differently according to their physical and chemical characteristics. Pollution-generated greenhouse gases will impact climate primarily through shortwave and longwave radiation, while aerosols can in addition affect climate through cloud–aerosol interactions.

Controls on anthropogenic emissions of methane (FAQ 8.2, Figure 1) to lower surface ozone have been identified as 'win–win' situations. Consequences of controlling other ozone precursors are not always as clear. NO_x emission controls, for instance, might be expected to have a cooling effect as they reduce tropospheric ozone, but their impact on CH_4 lifetime and aerosol formation is more likely instead to cause overall warming.

Satellite observations have identified increasing atmospheric concentrations of SO_2 (the primary precursor to scattering sulphate aerosols) from coal-burning power plants over eastern Asia during the last few decades. The most recent power plants use scrubbers to reduce such emissions (albeit not the concurrent CO_2 emissions and associated long-term climate warming). This improves air quality, but also reduces the cooling effect of sulphate aerosols and therefore exacerbates warming. Aerosol cooling occurs through aerosol–radiation and aerosol–cloud interactions and is estimated at –0.9 W m^{-2} (all aerosols combined, Section 8.3.4.3) since pre-industrial, having grown especially during the second half of the 20th century when anthropogenic emissions rose sharply. *(continued on next page)*

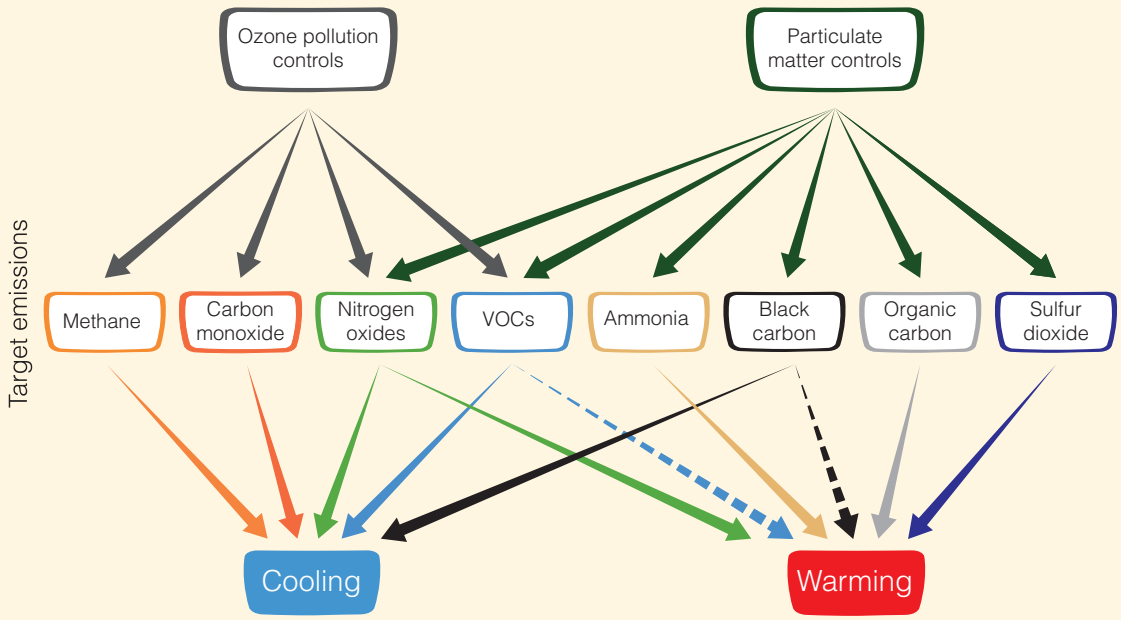

FAQ 8.2, Figure 1 | Schematic diagram of the impact of pollution controls on specific emissions and climate impact. Solid black line indicates known impact; dashed line indicates uncertain impact.

FAQ 8.2 (continued)

Black carbon or soot, on the other hand, absorbs heat in the atmosphere (leading to a 0.4 W m^{-2} radiative forcing from anthropogenic fossil and biofuel emissions) and, when deposited on snow, reduces its albedo, or ability to reflect sunlight. Reductions of black carbon emissions can therefore have a cooling effect, but the additional interaction of black carbon with clouds is uncertain and could lead to some counteracting warming.

Air quality controls might also target a specific anthropogenic activity sector, such as transportation or energy production. In that case, co-emitted species within the targeted sector lead to a complex mix of chemistry and climate perturbations. For example, smoke from biofuel combustion contains a mixture of both absorbing and scattering particles as well as ozone precursors, for which the combined climate impact can be difficult to ascertain.

Thus, surface air quality controls will have some consequences on climate. Some couplings between the targeted emissions and climate are still poorly understood or identified, including the effects of air pollutants on precipitation patterns, making it difficult to fully quantify these consequences. There is an important twist, too, in the potential effect of climate change on air quality. In particular, an observed correlation between surface ozone and temperature in polluted regions indicates that higher temperatures from climate change alone could worsen summertime pollution, suggesting a 'climate penalty'. This penalty implies stricter surface ozone controls will be required to achieve a specific target. In addition, projected changes in the frequency and duration of stagnation events could impact air quality conditions. These features will be regionally variable and difficult to assess, but better understanding, quantification and modelling of these processes will clarify the overall interaction between air pollutants and climate.

One reason an expert judgment estimate of ERF due to aerosol–radiation and aerosol–cloud interaction is provided rather than ERF due to aerosol–cloud interaction specifically is that the individual contributions are very difficult to disentangle. These contributions are the response of processes that are the outputs from a system that is constantly readjusting to multiple nonlinear forcings. Assumptions of independence and linearity are required to deduce ERF due to aerosol–radiation interaction and ERF due to aerosol–cloud interaction (although there is no *a priori* reason why the individual ERFs should be simply additive). Under these assumptions, ERF due to aerosol–cloud interaction is deduced as the difference between ERF due to aerosol–radiation and aerosol–cloud interaction and ERF due to aerosol–radiation interaction alone. This yields an ERF due to aerosol–cloud interaction estimate of –0.45 W m^{-2} which is much smaller in magnitude than the –1.4 W m^{-2} median forcing value of the models summarized in Figure 7.19 and is also smaller in magnitude than the AR4 estimates of –0.7 W m^{-2} for RF due to aerosol–cloud interaction.

8.3.4.4 Black Carbon Deposition in Snow and Ice

Because absorption by ice is very weak at visible and ultraviolet (UV) wavelengths, BC in snow makes the snow darker and increases absorption. This is not enough darkening to be seen by eye, but it is enough to be important for climate (Warren and Wiscombe, 1980; Clarke and Noone, 1985). Several studies since AR4 have re-examined this issue and find that the RF may be weaker than the estimates of Hansen and Nazarenko (2004) in AR4 (Flanner et al., 2007; Koch et al., 2009a; Rypdal et al., 2009; Lee et al., 2013). The anthropogenic BC on snow/ice is assessed to have a positive global and annual mean RF of +0.04 W m^{-2}, with a 0.02–0.09 W m^{-2} 5 to 95% uncertainty range (see further description in Section 7.5.2.3). This RF has a two to four times larger global mean surface temperature change per unit forcing than a change in CO_2.

In Figure 8.8, the time evolution of global mean RF due to BC on snow and ice is shown based on multi-model simulations in ACCMIP (Lee et al., 2013) for 1850, 1930, 1980 and 2000. The results show a maximum in the RF in 1980 with a small increase since 1850 and a 20% lower RF in 2000 compared to 1980. Those results are supported by observations. The BC concentration in the Arctic atmosphere is observed to be declining since 1990, at least in the Western Hemisphere portion (Sharma et al., 2004), which should lead to less deposition of BC on the snow surface. Surveys across Arctic during 1998 and 2005 to 2009 showed that the BC content of Arctic snow appears to be lower than in 1984 (Doherty et al., 2010) and found BC concentrations in Canada, Alaska and the Arctic Ocean (e.g., Hegg et al., 2009), about a factor of 2 lower than measured in the 1980s (e.g., Clarke and Noone, 1985). Large-area field campaigns (Huang et al., 2011; Ye et al., 2012) found that the BC content of snow in northeast China is comparable to values found in Europe. The steep drop off in BC content of snow with latitude in northeast China may indicate that there is not much BC in the Arctic coming from China (Huang et al., 2011; Ye et al., 2012; Wang et al., 2013). The change in the spatial pattern of emission of BC is a main cause for the difference in the temporal development of RF due to BC on snow and ice compared to the BC from RF due to aerosol–radiation interaction over the last decades.

8.3.4.5 Contrails and Contrail-Induced Cirrus

AR4 assessed the RF of contrails (persistent linear contrails) as +0.01 (–0.007 to +0.02) W m^{-2} and provided no estimate for contrail induced cirrus. In AR5, Chapter 7 gives a best estimate of RF due to contrails of +0.01 (+0.005 to +0.03) W m^{-2} and an ERF estimate of the combined contrails and contrail-induced cirrus of +0.05 (+0.02 to +0.15) W m^{-2}. Since AR4, the evidence for contrail-induced cirrus has increased because of observational studies (for further details see Section 7.2.7).

8.3.5 Land Surface Changes

8.3.5.1 Introduction

Anthropogenic land cover change has a direct impact on the Earth radiation budget through a change in the surface albedo. It also impacts the climate through modifications in the surface roughness, latent heat flux and river runoff. In addition, human activity may change the water cycle through irrigation and power plant cooling, and also generate direct input of heat to the atmosphere by consuming energy. Land use change, and in particular deforestation, also has significant impacts on WMGHG concentration, which are discussed in Section 6.3.2.2. Potential geo-engineering techniques that aim at increasing the surface albedo are discussed in Section 7.7.2.3.

AR4 referenced a large number of RF estimates resulting from a change in land cover albedo. It discussed the uncertainties due to the reconstruction of historical vegetation, the characterization of present-day vegetation and the surface radiation processes. On this basis, AR4 gave a best estimate of RF relative to 1750 due to land use related surface albedo at –0.2 ± 0.2 W m^{-2} with a level of scientific understanding at medium-low.

8.3.5.2 Land Cover Changes

Hurtt et al. (2006) estimates that 42 to 68% of the global land surface was impacted by land use activities (crop, pasture, wood harvest) during the 1700–2000 period. Until the mid-20th century most land use change took place over the temperate regions of the NH. Since then, reforestation is observed in Western Europe, North America and China as a result of land abandonment and afforestation efforts, while deforestation is concentrated in the tropics. After a rapid increase of the rate of deforestation during the 1980s and 1990s, satellite data indicate a slowdown in the past decade (FAO, 2012).

Since AR4, Pongratz et al. (2008) and Kaplan et al. (2011) extended existing reconstructions on land use back in time to the past millennium, accounting for the progress of agriculture technique and historical events such as the black death or war invasions. As agriculture was already widespread over Europe and South Asia by 1750, the RF, which is defined with respect to this date, is weaker than the radiative flux change from the state of natural vegetation cover (see Figure 8.9). Deforestation in Europe and Asia during the last millennium led to a significant regional negative forcing. Betts et al. (2007) and Goosse et al. (2006) argue that it probably contributed to the 'Little Ice Age', together with natural solar and volcanic activity components, before the increase in GHG concentration led to temperatures similar to those experienced in the early part of the second millennium. There is still significant uncertainty in the anthropogenic land cover change, and in particular its time evolution (Gaillard et al., 2010).

8.3.5.3 Surface Albedo and Radiative Forcing

Surface albedo is the ratio between reflected and incident solar flux at the surface. It varies with the surface cover. Most forests are darker (i.e., lower albedo) than grasses and croplands, which are darker than barren land and desert. As a consequence, deforestation tends to increase the Earth albedo (negative RF) while cultivation of some bright surfaces may have the opposite effect. Deforestation also leads to a large increase in surface albedo in case of snow cover as low vegetation accumulates continuous snow cover more readily in early winter allowing it to persist longer in spring. This causes average winter albedo in deforested areas to be generally much higher than that of a tree-covered landscape (Bernier et al., 2011).

The pre-industrial impact of the Earth albedo increase due to land use change, including the reduced snow masking by tall vegetation, is estimated to be on the order of –0.05 W m^{-2} (Pongratz et al., 2009). Since then, the increase in world population and agriculture development led to additional forcing. Based on reconstruction of land use since the beginning of the Industrial Era, Betts et al. (2007) and Pongratz et al. (2009) computed spatially and temporally distributed estimates of the land use RF. They estimate that the shortwave flux change induced by the albedo variation, from fully natural vegetation state to 1992, is on the order of –0.2 W m^{-2} (range –0.24 to –0.21W m^{-2}). The RF, defined with respect to 1750, is in the range –0.17 to –0.18 W m^{-2}. A slightly stronger value (–0.22 W m^{-2}) was found by Davin et al. (2007) for the period 1860–1992.

In recent years, the availability of global scale MODIS data (Schaaf et al., 2002) has improved surface albedo estimates (Rechid et al., 2009). These data have been used by Myhre et al (2005a) and Kvalevag et al. (2010). They argue that the observed albedo difference between natural vegetation and croplands is less than usually assumed in climate simulations, so that the RF due to land use change is weaker than in estimates that do not use the satellite data. On the other hand, Nair et al. (2007) show observational evidence of an underestimate of the surface albedo change in land use analysis in southwest Australia. Overall, there is still a significant range of RF estimates for the albedo component of land use forcing. This is mostly due to the range of albedo change as a result of land use change, as shown in an inter-comparison of seven atmosphere–land models (de Noblet-Ducoudre et al., 2012).

Deforestation has a direct impact on the atmospheric CO_2 concentration and therefore contributes to the WMGHG RF as quantified in Section 8.3.2. Conversely, afforestation is a climate mitigation strategy to limit the CO_2 concentration increase. Several authors have compared the radiative impact of deforestation/afforestation that results from the albedo change with the greenhouse effect of CO_2 released/sequestered. Pongratz et al. (2010) shows that the historic land use change has had a warming impact (i.e., greenhouse effect dominates) at the global scale and over most regions with the exception of Europe and India. Bala et al. (2007) results show latitudinal contrast where the greenhouse effect dominates for low-latitude deforestation while

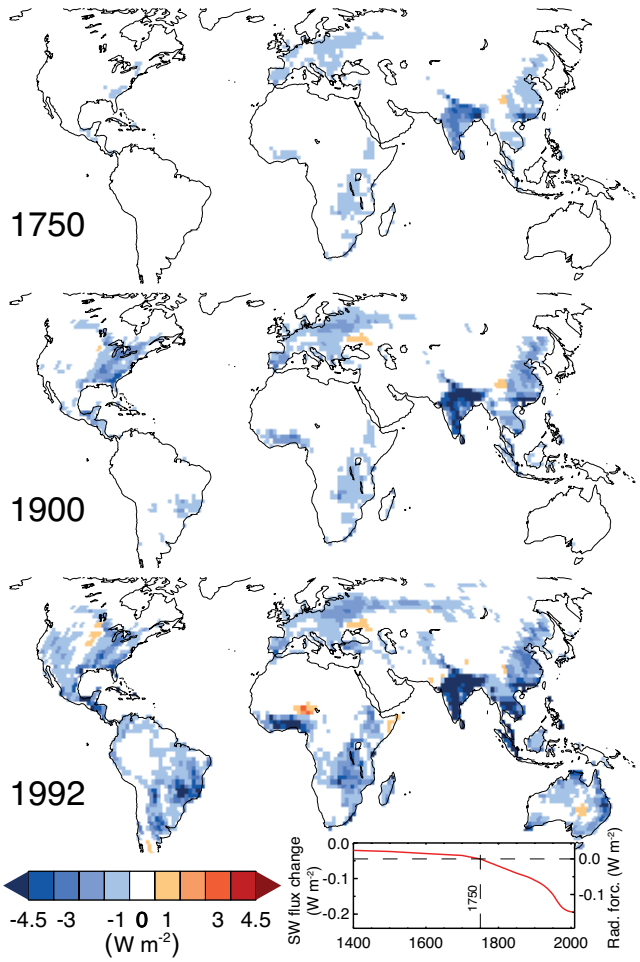

Figure 8.9 | Change in top of the atmosphere (TOA) shortwave (SW) flux (W m^{-2}) following the change in albedo as a result of anthropogenic Land Use Change for three periods (1750, 1900 and 1992 from top to bottom). By definition, the RF is with respect to 1750, but some anthropogenic changes had already occurred in 1750. The lower right inset shows the globally averaged impact of the surface albedo change to the TOA SW flux (left scale) as well as the corresponding RF (right scale) after normalization to the 1750 value. Based on simulations by Pongratz et al. (2009).

the combined effect of albedo and evapotranspiration impact does at high latitude. These results are also supported by Bathiany et al. (2010). Similarly, Lohila et al. (2010) shows that the afforestation of boreal peatlands results in a balanced RF between the albedo and greenhouse effect. Overall, because of the opposite impacts, the potential of afforestation to mitigate climate change is limited (Arora and Montenegro, 2011) while it may have undesired impacts on the atmospheric circulation, shifting precipitation patterns (Swann et al., 2012).

8.3.5.4 Other Impacts of Land Cover Change on the Earth's Albedo

Burn scars resulting from agriculture practices, uncontrolled fires or deforestation (Bowman et al., 2009) have a lower albedo than unperturbed vegetation (Jin and Roy, 2005). On the other hand, at high latitude, burnt areas are more easily covered by snow, which may result in an overall increase of the surface albedo. Surface blackening of natural vegetation due to fire is relatively short lived and typically disappears within one to a few years (Jin et al., 2012). Myhre et al. (2005b) estimates a global albedo-related radiative effect due to African fires of 0.015 W m^{-2}.

Over semi-arid areas, the development of agriculture favours the generation of dust. Mulitza et al. (2010) demonstrates a very large increase of dust emission and deposition in the Sahel concomitant with the development of agriculture in this area. This, together with the analysis of dust sources (Ginoux et al., 2010), suggests that a significant fraction of the dust that is transported over the Atlantic has an anthropogenic origin and impacts the Earth albedo. There is no full estimate of the resulting RF, however. The dust RF estimate in Section 8.3.4.2 includes both land use contributions and change in wind-driven emissions. Both dust and biomass burning aerosol may impact the Earth surface albedo as these particles can be deposed on snow, which has a large impact on its absorption, in particular for soot. This is discussed in Section 8.3.4.4.

Urban areas have an albedo that is 0.01 to 0.02 smaller than adjacent croplands (Jin et al., 2005). There is the potential for a strong increase through white roof coating with the objective of mitigating the heat island effect (Oleson et al., 2010). Although the global scale impact is small, local effects can be very large, as shown by Campra et al. (2008) that reports a regional (260 km^2) 0.09 increase in albedo and –20 W m^{-2} RF as a consequence of greenhouse horticulture development.

8.3.5.5 Impacts of Surface Change on Climate

Davin et al. (2007) argues that the climate sensitivity to land use forcing is lower than that for other forcings, due to its spatial distribution but also the role of non-radiative processes. Indeed, in addition to the impact on the surface albedo, land use change also modifies the evaporation and surface roughness, with counterbalancing consequences on the lower atmosphere temperature. There is increasing evidence that the impact of land use on evapotranspiration—a non-RF on climate—is comparable to, but of opposite sign than, the albedo effect, so that RF is not as useful a metric as it is for gases and aerosols. For instance, Findell et al. (2007) climate simulations show a negligible impact of land use change on the global mean temperature, although there are some significant regional changes.

Numerical climate experiments demonstrate that the impact of land use on climate is much more complex than just the RF. This is due in part to the very heterogeneous nature of land use change (Barnes and Roy, 2008), but mostly due to the impact on the hydrological cycle through evapotranspiration, root depth and cloudiness (van der Molen et al., 2011). As a consequence, the forcing on climate is not purely radiative and the net impact on the surface temperature may be either positive or negative depending on the latitude (Bala et al., 2007). Davin and de Noblet-Ducoudre (2010) analyses the impact on climate of large-scale deforestation; the albedo cooling effect dominates for high latitude whereas reduced evapotranspiration dominates in the tropics. This latitudinal trend is confirmed by observations of the temperature difference between open land and nearby forested land (Lee et al., 2011).

Irrigated areas have continuously increased during the 20th century although a slowdown has been observed in recent decades (Bonfils

and Lobell, 2007). There is clear evidence that irrigation leads to local cooling of several degrees (Kueppers et al., 2007). Irrigation also affects cloudiness and precipitation (Puma and Cook, 2010). In the United States, DeAngelis et al. (2010) found that irrigation in the Great Plains in the summer produced enhanced precipitation in the Midwest 1000 km to the northeast.

8.3.5.6 Conclusions

There is still a rather wide range of estimates of the albedo change due to anthropogenic land use change, and its RF. Although most published studies provide an estimate close to –0.2 W m^{-2}, there is convincing evidence that it may be somewhat weaker as the albedo difference between natural and anthropogenic land cover may have been overestimated. In addition, non-radiative impact of land use have a similar magnitude, and may be of opposite sign, as the albedo effect (though these are not part of RF). A comparison of the impact of land use change according to seven climate models showed a wide range of results (Pitman et al., 2009), partly due to difference in the implementation of land cover change, but mostly due to different assumptions on ecosystem albedo, plant phenology and evapotranspiration. There is no agreement on the sign of the temperature change induced by anthropogenic land use change. It is *very likely* that land use change led to an increase of the Earth albedo with a RF of –0.15 ± 0.10 W m^{-2}, but a net cooling of the surface—accounting for processes that are not limited to the albedo—is *about as likely as not*.

8.4 Natural Radiative Forcing Changes: Solar and Volcanic

Several natural drivers of climate change operate on multiple time scales. Solar variability takes place at many time scales that include centennial and millennial scales (Helama et al., 2010), as the radiant energy output of the Sun changes. Also, variations in the astronomical alignment of the Sun and the Earth (Milankovitch cycles) induce cyclical changes in RF, but this is substantial only at millennial and longer time scales (see Section 5.2.1.1). Volcanic forcing is highly episodic, but can have dramatic, rapid impacts on climate. No major asteroid impacts occurred during the reference period (1750–2012) and thus this effect is not considered here. This section discusses solar and volcanic forcings, the two dominant natural contributors of climate change since the pre-industrial time.

8.4.1 Solar Irradiance

In earlier IPCC reports the forcing was estimated as the instantaneous RF at TOA. However, due to wavelength-albedo dependence, solar radiation-wavelength dependence and absorption within the stratosphere and the resulting stratospheric adjustment, the RF is reduced to about 78% of the TOA instantaneous RF (Gray et al., 2009). There is *low confidence* in the exact value of this number, which can be model and time scale dependent (Gregory et al., 2004; Hansen et al., 2005). AR4 gives an 11-year running mean instantaneous TOA RF between 1750 and the present of 0.12 W m^{-2} with a range of estimates of 0.06 to 0.30 W m^{-2}, equivalent to a RF of 0.09 W m^{-2} with a range of 0.05 to 0.23 W m^{-2}. For a consistent treatment of all forcing agents, hereafter we use RF while numbers quoted from AR4 will be provided both as RF and instantaneous RF at TOA.

8.4.1.1 Satellite Measurements of Total Solar Irradiance

Total solar irradiance (TSI) measured by the Total Irradiance Monitor (TIM) on the spaceborne Solar Radiation and Climate Experiment (SORCE) is 1360.8 ± 0.5 W m^{-2} during 2008 (Kopp and Lean, 2011) which is ~4.5 W m^{-2} lower than the Physikalisch-Meteorologisches Observatorium Davos (PMOD) TSI composite during 2008 (Frohlich, 2009).The difference is probably due to instrumental biases in measurements prior to TIM. Measurements with the PREcision MOnitor Sensor (PREMOS) instrument support the TIM absolute values (Kopp and Lean, 2011). The TIM calibration is also better linked to national standards which provides further support that it is the most accurate (see Supplementary Material Section 8.SM.6). Given the lower TIM TSI values relative to currently used standards, most general circulation models are calibrated to incorrectly high values. However, the few tenths of a percent bias in the absolute TSI value has minimal consequences for climate simulations because the larger uncertainties in cloud properties have a greater effect on the radiative balance. As the maximum-to-minimum TSI relative change is well-constrained from observations, and historical variations are calculated as changes relative to modern values, a revision of the absolute value of TSI affects RF by the same fraction as it affects TSI. The downward revision of TIM TSI with respect to PMOD, being 0.3%, thus has a negligible impact on RF, which is given with a relative uncertainty of several tenths of a percent.

Since 1978, several independent space-based instruments have directly measured the TSI. Three main composite series were constructed, referred to as the Active Cavity Radiometer Irradiance Monitor (ACRIM) (Willson and Mordvinov, 2003), the Royal Meteorological Institute of Belgium (RMIB) (Dewitte et al., 2004) and the PMOD (Frohlich, 2006) series. There are two major differences between ACRIM and PMOD. The first is the rapid drift in calibration between PMOD and ACRIM before 1981. This arises because both composites employ the Hickey–Frieden (HF) radiometer data for this interval, while a re-evaluation of the early HF degradation has been implemented by PMOD but not by ACRIM. The second one, involving also RMIB, is the bridging of the gap between the end of ACRIM I (mid-1989) and the beginning of ACRIM II (late 1991) observations, as it is possible that a change in HF data occurred during this gap. This possibility is neglected in ACRIM and thus its TSI increases by more than 0.5 W m^{-2} during solar cycle (SC) 22. These differences lead to different long-term TSI trends in the three composites (see Figure 8.10): ACRIM rises until 1996 and subsequently declines, RMIB has an upward trend through 2008 and PMOD shows a decline since 1986 which unlike the other two composites, follows the solar-cycle-averaged sunspot number (Lockwood, 2010). Moreover, the ACRIM trend implies that the TSI on time scales longer than the SC is positively correlated with the cosmic ray variation indicating a decline in TSI throughout most of the 20th century (the opposite to most TSI reconstructions produced to date; see Section 8.4.1.2). Furthermore, extrapolating the ACRIM TSI long-term drift would imply a brighter Sun in the Maunder minimum (MM) than now, again opposite to most TSI reconstructions (Lockwood and Frohlich, 2008). Finally, analysis of instrument degradation and pointing issues (Lee et al., 1995) and independent modeling based on solar magnetograms (Wenzler et al.,